IEEE Access
Multidisciplinary ⋮ Rapid Review ⋮ Open Access Journal

Received 9 January 2023, accepted 23 January 2023, date of publication 27 January 2023, date of current version 1 February 2023.

Digital Object Identifier 10.1109/ACCESS.2023.3240310

RESEARCH ARTICLE

Research on Control Strategy of Solid State Transformer Based on Improved MPC Method

CAN DING, HONGRONG ZHANG, YUNWEN CHEN, AND GUANG PU
College of Electrical Engineering and New Energy, China Three Gorges University, Yichang 443002, China
Corresponding author: Hongrong Zhang (zhanghongrong@ctgu.edu.cn)

ABSTRACT As the core equipment of smart grid, solid-state transformer (SST) needs to have good power quality regulation capability under grid side faults and load side faults. To ensure that the high-voltage side converter works at unity power factor and smooth DC voltage. At the same time, the three-phase output voltages need to have high steady-state accuracy and strong anti-interference capability. In this paper, an improved model predictive control scheme was proposed. First, a theoretical modeling analysis of the high and low voltage side of a solid-state transformer was performed. Then, power and voltage prediction models are developed for the high-voltage side converter and low-voltage side converter of the SST, respectively. Three voltage vectors are selected for prediction by the cost function, and the equivalent voltage vector in the two-phase stationary coordinate system is synthesized and modulated to control the converter. Finally, simulation was conducted to compare and analyze various operating conditions of SST under different control schemes. The control effect of solid-state transformer under improved model predictive control is better than traditional finite control set model predictive control and proportional integral control, which can better regulate power quality.

INDEX TERMS Solid-state transformer, model predictive control, three-vector, two-phase stationary coordinate system.

I. INTRODUCTION

Solid state transformer (SST), as a new type of intelligent power conversion equipment, is the core of microgrid control. The flexible control and easy expansion characteristics of SST allow it to be used as the basic control unit of microgrid to realize energy management and plug-and-play [1], [2], [3].

SST can be divided into two categories by topology: with DC bus and without DC bus. The control of the converter with the high and low voltage sides of the DC link SST is more flexible. Compared with the non-DC bus SST, the SST with DC bus has the following advantages:1) it can achieve unity power factor operation; 2) it can realize bidirectional energy flow [4]; and 3) it have a certain suppression of voltage and current harmonics. Considering the limitation of the rated voltage of the equipment, the SST in the medium and high voltage fields mostly adopt the modular cascade topology or multilevel converters [5], [6]. The modular cascade topology in [6] has the limitation of voltage and power imbalance between modules, which can be controlled by the voltage and power equalization strategy, but it will greatly increase the complexity of the control system. Silicon Carbide (SiC)-based power electronics proposed in [7], [8], and [9] make the topology of high-voltage, large-capacity SST simpler.

The SST comprises a voltage-source rectifier, an isolated DC/DC converter and a voltage-source inverter. Among them, the DC/DC converter allows bidirectional transmission of electric energy and adopts a phase-shift control strategy [10]. The conventional control method of rectifiers and inverters is voltage-oriented control strategy [11], [12]. In this case, the decoupled dq axis components are controlled by the proportional integral (PI) controllers, which provide zero steady-state error. Nonetheless, the PI controllers suffer from integral saturation and difficult parameter adjustment, raising the complexity of the design [13]. Model predictive control, on the other hand, is characterized by easy consideration

The associate editor coordinating the review of this manuscript and approving it for publication was Chi-Seng Lam.

of nonlinearities and constraints, fast response, etc [14]. Among them, finite control set model predictive control (FCS-MPC) considers the finiteness of control input values generated by power valve switching actions in power electronics. It transforms the control problem into an optimization problem by building a system cost function. This control method is widely used, such as magnet synchronous motor drives [15], HVDC transmission [16], and converters control [17], [18]. In [19], model predictive control is used for AC/AC type matrix SST using a virtual DC loop. In [20], the multi-objective model predictive control of multi-level three-phase cascade SST is studied, which has reference significance for the model predictive control of AC/DC/AC type SST.

FCS-MPC selects the voltage vector that minimizes the cost function as the optimal voltage vector. However, since the selectable voltage vectors are limited to eight, the direction and amplitude of the voltage vectors from the converter are fixed. The algorithm has high current pulsation and variable switching frequency, which will make the filter design more difficult and result in poor system performance [21], [22], [23]. In addition, in order to maintain a good control effect, the system needs a higher sampling frequency. In [24], and [25], combined with optimal voltage vector selection and modulation, single-vector and dual-vector model predictive control for grid-connected converters were proposed, respectively. Among them, dual vector predictive control applies non-zero vector and zero vector in each control cycle. However, these two kinds of control cannot theoretically eliminate the steady-state error, thereby improving the control accuracy [26].

The Three-Vector Model Predictive Control (TV-MPC) proposed in this paper uses the grid side power and the output-side voltage as the predictive model for the high-voltage side converter and low-voltage side converter, respectively. The two active-vectors that make the cost function the smallest and the second-smallest respectively are found and their corresponding action times are calculated. Finally, the two active vectors and the zero vector and their corresponding times are synthesized to obtain the switching state. The TV-MPC control uses three vectors in one control cycle, and considers the combination of various switching states. Compared with FCS-MPC, it can suppress harmonics and disturbances more effectively. It reduces the switching frequency and keeps it fixed. The effectiveness of the proposed strategy is verified under five conditions: steady-state operation, grid side voltages unbalance, grid side voltages contain harmonics, three-phase short circuit on the load side, and loads suddenly change.

II. MATHEMATICAL MODEL OF SST

A. RECTIFIER STAGE

The topology structure and control block diagram of SST are shown in Fig. 1, where R_s is the source grid resistance, L_s is the source grid inductance, U_{dc1} is the HVDC bus voltage, U_{dc2} is the LVDC bus voltage, C_1 is the HVDC bus capacitor, C_2 is the LVDC bus capacitor. The LC filter with resistance R_f, inductance L_f and capacitance C_f is located at the output side of SST. Similarly, I_f is the filter currents, U_o is the output voltages, I_o is the output currents, and Z_{load} is the three-phase loads.

According to the KCL and KVL, the mathematical model of the SST rectifier stage can be obtained:

$$L_s \frac{\mathrm{d}\boldsymbol{I}_g}{\mathrm{d}t} + R_s \boldsymbol{I}_g = \boldsymbol{U}_g - \boldsymbol{U}_{in} \tag{1}$$

where $\boldsymbol{U}_g = \begin{bmatrix} U_{ga} & U_{gb} & U_{gc} \end{bmatrix}^{\mathrm{T}}$ is the vector of grid side voltages, $\boldsymbol{I}_g = \begin{bmatrix} I_{ga} & I_{gb} & I_{gc} \end{bmatrix}^{\mathrm{T}}$ is the vector of grid side currents, $\boldsymbol{U}_{in} = \begin{bmatrix} U_{ina} & U_{inb} & U_{inc} \end{bmatrix}^{\mathrm{T}}$ is the vector of the high-voltage side converter input voltage.

The model is established in the three-phase stationary frame. In order to simplify the design of the control system, coordinate transformation is used to convert the system model in the three-phase stationary reference frame to the d-q reference frame. After the transformation, the mathematical model of the rectifier stage can be expressed as:

$$\begin{cases} L_s \frac{\mathrm{d}I_{gd}}{\mathrm{d}t} &= -R_s I_{gd} + \omega L_s I_{gq} + U_{gd} - U_{ind} \\ L_s \frac{\mathrm{d}I_{gq}}{\mathrm{d}t} &= -R_s I_{gq} - \omega L_s I_{gd} + U_{gq} - U_{inq} \end{cases} \tag{2}$$

where U_{gd}, U_{gq} and I_{gd}, I_{gq} and U_{ind}, U_{inq} are the components of $\boldsymbol{U}_g$, $\boldsymbol{I}_g$ and $\boldsymbol{U}_{in}$ under the d-q reference frame respectively.

According to the the Euler Forward method in (3):

$$\frac{\mathrm{d}I}{\mathrm{d}t} = \frac{I(k+1) - I(k)}{T_s} \tag{3}$$

the predicted value of grid side currents at the $(k+1)$th time can be obtained by transforming (3) as shown in (4).

$$\begin{cases} I_{gd}(k+1) = (1 - \frac{T_s R_s}{L_s}) I_{gd}(k) \\ + \frac{T_s}{L_s}(U_{gd}(k) - U_{ind}(k) + \omega L_s I_{gq}(k)) \\ I_{gq}(k+1) = (1 - \frac{T_s R_s}{L_s}) I_{gq}(k) \\ + \frac{T_s}{L_s}(U_{gq}(k) - U_{inq}(k) - \omega L_s I_{gd}(k)) \end{cases} \tag{4}$$

Since the sampling period T_s is much smaller than the period of the grid side voltage, it is considered that the grid side voltages are the same in the two adjacent sampling periods, which can be expressed as:

$$\begin{cases} U_{gd}(k+1) &= U_{gd}(k) \\ U_{gq}(k+1) &= U_{gq}(k) \end{cases} \tag{5}$$

According to the instantaneous power theory, we can get:

$$\begin{cases} p(k+1) = \frac{3}{2}(U_{gd}(k+1) I_{gd}(k+1) \\ + U_{gq}(k+1) I_{gq}(k+1)) \\ q(k+1) = \frac{3}{2}(U_{gq}(k+1) I_{gd}(k+1) \\ - U_{gd}(k+1) I_{gq}(k+1)) \end{cases} \tag{6}$$

where $p(k+1)$ and $q(k+1)$ are the predicted value of the grid side power at the $(k+1)$th instant time.

Defining the switching state S_a, S_b, S_c, where $S_k(k = a, b, c)$ is taken as shown in (7), and S_{k1} and S_{k2} are the switching states of the upper and lower bridge arms of the kth phase of the SST converters, respectively.

$$S_k = \begin{cases} 1\ S_{k1}\ \text{on}, & S_{k2}\ \text{off} \\ 0\ S_{k1}\ \text{off}, & S_{k2}\ \text{on} \end{cases} \tag{7}$$

The admissible switching states $\boldsymbol{u}$ are within a finite set (See Fig. 3)

$$u \in \mu = \{u_0(000), u_1(001), \ldots, u_6(101), u_7(111)\} \tag{8}$$

B. INVERTER STAGE

According to KVL, the current equation of the three-phase filter inductor is obtained:

$$L_f \frac{\mathrm{d}\boldsymbol{I}_f}{\mathrm{d}t} = \boldsymbol{U}_i - \boldsymbol{U}_o - R_f \boldsymbol{I}_f \tag{9}$$

where $\boldsymbol{I}_f = \left[I_{fa}\ I_{fb}\ I_{fc}\right]^{\mathrm{T}}$ is the vector of currents flowing through the inductors, $\boldsymbol{U}_i = \left[U_{ia}\ U_{ib}\ U_{ic}\right]^{\mathrm{T}}$ is the vector of the inverter bridge midpoint voltages, $\boldsymbol{U}_o = \left[U_{oa}\ U_{ob}\ U_{oc}\right]^{\mathrm{T}}$ is the vector of output voltages.

According to KCL, the voltage equation of the three-phase filter capacitor is obtained:

$$C_f \frac{\mathrm{d}\boldsymbol{U}_o}{\mathrm{d}t} = \boldsymbol{I}_f - \boldsymbol{I}_o \tag{10}$$

where $\boldsymbol{I_o} = \left[I_{oa}\ I_{ob}\ I_{oc}\right]^{\mathrm{T}}$ is the vector of the output currents.

Combining (9) and (10), the state equation of the SST inverter stage can be obtained as:

$$\begin{cases} \frac{\mathrm{d}\boldsymbol{I}_f}{\mathrm{d}t} = \frac{1}{L_f}\boldsymbol{U}_i - \frac{1}{L_f}\boldsymbol{U}_o - \frac{R_f}{L_f}\boldsymbol{I}_f \\ \frac{\mathrm{d}\boldsymbol{U}_o}{\mathrm{d}t} = \frac{1}{C_f}\boldsymbol{I}_f - \frac{1}{C_f}\boldsymbol{I}_o \end{cases} \tag{11}$$

The Clark transformation of the inverter mathematical model yields the equation of state as:

$$\begin{cases} \dot{\boldsymbol{x}} = \boldsymbol{A}\boldsymbol{x} + \boldsymbol{B}\boldsymbol{U}_{i\alpha\beta} + \boldsymbol{B}_i\boldsymbol{I}_{o\alpha\beta} \\ \boldsymbol{y} = \boldsymbol{C}\boldsymbol{x} \end{cases} \tag{12}$$

where $\boldsymbol{x} = \left[\boldsymbol{I}_{f\alpha\beta}\ \boldsymbol{U}_{o\alpha\beta}\right]^{\mathrm{T}}$ is the state variable matrix, $\boldsymbol{U}_{i\alpha\beta}$ is the input vector, $\boldsymbol{I}_{o\alpha\beta}$ is the system disturbance vector, and $\boldsymbol{y}$ is the output vector.

$\boldsymbol{A} = \begin{bmatrix} -\frac{R_f}{L_f} & -\frac{1}{L_f} \\ \frac{1}{C_f} & 0 \end{bmatrix}$ is state matrix, $\boldsymbol{B} = \left[\frac{1}{L_f}\ 0\right]^{\mathrm{T}}$ is input matrix, $\boldsymbol{B}_i = \left[0\ -\frac{1}{C_f}\right]^{\mathrm{T}}$ is perturbation matrix, $\boldsymbol{C} = \left[0\ 1\right]$is output matrix.

III. CONTROL METHODS FOR SST

A. VOLTAGE-ORIENTED PI CONTROL

Voltage-Oriented PI Control is a classic control method for power converters. The control structure is shown in Fig. 2. The outer loop regulates the dc link voltage to a constant reference U^*_{dc1}. The inner loops control the active and reactive currents under the d-q reference frame. Decoupling terms are added to the Pl controller to decouple the d axis and q axis current dynamics.

B. FCS-MPC CONTROL

FCS-MPC is based on the minimization of a defined cost function for all eight switching states $\boldsymbol{u}$ by using the prediction model (6). To achieve unity power factor operation, the reference value of reactive power q_{ref} is set to zero. The reference value of active power p_{ref} comes from an outer DC-link voltage controller. The cost function can be defined as:

$$g_r = (p_{ref} - p(k+1))^2 + (q_{ref} - q(k+1))^2 \tag{13}$$

However, only one of the original eight fundamental vectors (the yellow lines in Fig. 3) is available to minimize the cost function. As a consequence, FCS-MPC does not fully make use of the converter control region.

C. THE PROPOSED TV-MPC

To cope with the drawback of FCS-MPC, a TV-MPC was proposed, instead of only one original fundamental vector in each period, an equivalent vector was synthesized with two active vectors and one zero vector. It allows for an extra freedom of the synthesized vector at an "arbitrary phase" with variable length. Therefore, the voltage vector range for TV-MPC is extended to the green area as illustrated in Fig. 3.The main ideas are as follows:

1) CALCULATING AND SORTING THE COST FUNCTIONS

The six active vectors and two zero vectors are substituted into (6) to calculate the predicted power values. And each power value is substituted into (13) in turn to get the corresponding cost function. Sorting the cost function obtained from the six active vectors, the smallest and the second-smallest cost function are selected. The switching states and vectors are shown in Table 1.

2) ACQUISITION OF THE BEST VECTOR AND THE SECOND-BEST VECTOR

The best vector and second-best vector can be deduced backwards from the smallest cost function and the second-smallest cost function. As shown in Fig. 3, the power reference corresponds to a reference voltage vector of $\boldsymbol{u}_{ref}$. When the reference voltage vector falls in sector I, then the blue and red line lengths in the figure represent the relative error of power tracking under the action of the active voltage vector. From Fig. 3, the power tracking error generated by $\boldsymbol{u}_1$ and $\boldsymbol{u}_2$ (red lines) are smaller than the power tracking error generated by the action of other active voltage vectors(blue lines). Therefore, the best vector and the second-best voltage vector are adjacent to each other.

3) ACTION TIME OF VOLTAGE VECTORS

In this paper, the action time for each of the vector is calculated from the cost function computed for each the switching state. From (13), it can be known that the cost function represents the power tracking error. Since the action time for each voltage vector is inversely proportional to the cost

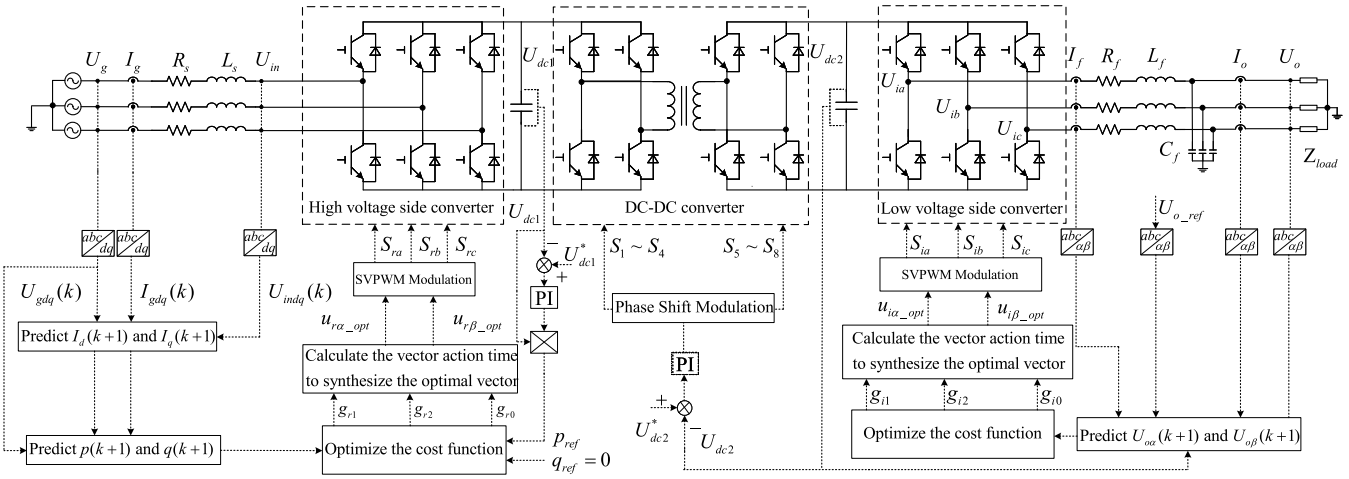

FIGURE 1. SST topology and control block diagram.

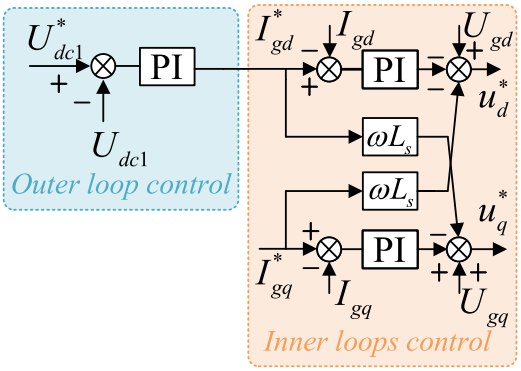

FIGURE 2. PI control principle diagram.

function, larger power tracking cost function leads to smaller action time for each voltage vector [27]. The action time of the best vector, the second-best vector and zero-vector are obtained as shown in (14):

$$\begin{cases} t_{r1} &= \frac{g_{r0}g_{r2}}{g_{r0}g_{r1}+g_{r0}g_{r2}+g_{r1}g_{r2}}T_s \\ t_{r2} &= \frac{g_{r0}g_{r1}}{g_{r0}g_{r1}+g_{r0}g_{r2}+g_{r1}g_{r2}}T_s \\ t_{r0} &= T_s - t_{r1} - t_{r2} \end{cases} \tag{14}$$

where g_{r1}, g_{r2} and g_{r0} are the smallest cost function, the second-smallest cost function and the zero-vector cost function, respectively.

4) SYNTHESIS OF EQUIVALENT VOLTAGE VECTOR

Through the selection of the three voltage vectors and the calculation of their corresponding action time, the synthesis of the equivalent voltage vector can be realized, as shown in (15).

$$\begin{cases} u_{r\alpha-eq} &= \frac{t_{r1}}{T_s}v_{\alpha1} + \frac{t_{r2}}{T_s}v_{\alpha2} \\ u_{r\beta-eq} &= \frac{t_{r1}}{T_s}v_{\beta1} + \frac{t_{r2}}{T_s}v_{\beta2} \end{cases} \tag{15}$$

Therefore, the equivalent voltage vector is closer to the voltage reference vector corresponding to the reference

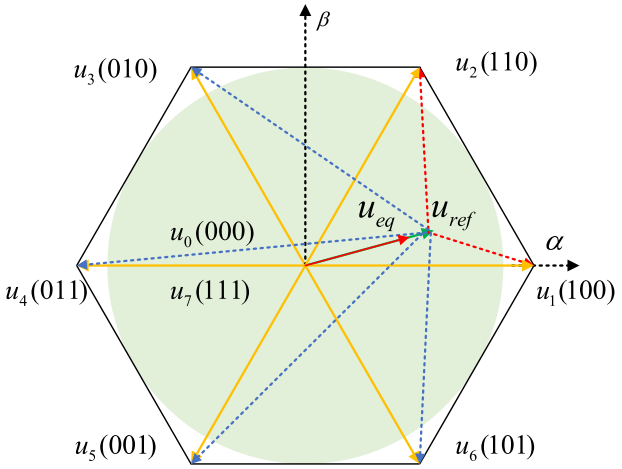

FIGURE 3. Voltage vector range for FCS-MPC,TV-MPC.

TABLE 1. Switching States and voltage vectors.

u_i	S_a	S_b	S_c	v_α	v_β
u_0	0	0	0	0	0
u_1	1	0	0	$\frac{2}{3}u_{dc}$	0
u_2	1	1	0	$\frac{1}{3}u_{dc}$	$\frac{\sqrt{3}}{3}u_{dc}$
u_3	0	1	0	$-\frac{1}{3}u_{dc}$	$\frac{\sqrt{3}}{3}u_{dc}$
u_4	0	1	1	$-\frac{2}{3}u_{dc}$	0
u_5	0	0	1	$-\frac{1}{3}u_{dc}$	$-\frac{\sqrt{3}}{3}u_{dc}$
u_6	1	0	1	$\frac{1}{3}u_{dc}$	$-\frac{\sqrt{3}}{3}u_{dc}$
u_7	1	1	1	0	0

power, the power tracking error is effectively reduced, and a better control effect is obtained.

D. INVERTER STAGE TV-MPC

In order to achieve a better control effect of the SST output voltages under steady-state operation and faults, the output voltages are predicted and controlled. Since model predictive

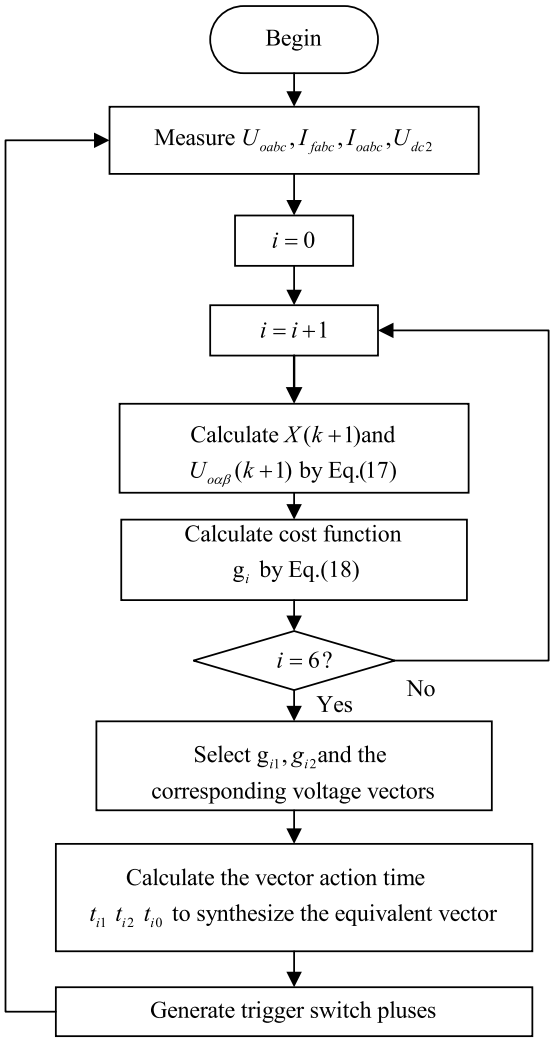

FIGURE 4. Inverter Stage TV-MPC flow chart.

control requires rolling optimization in the time domain, (12) needs to be discretized. In the case where the sampling period is small enough, the discrete model, based on a zero-order holder, can be obtained:

$$\begin{cases} \boldsymbol{X}(k+1) & = \boldsymbol{A}_q \boldsymbol{X}(k) + \boldsymbol{B}_p \boldsymbol{U}_{i\alpha\beta}(k) + \boldsymbol{B}_{dp} \boldsymbol{I}_{o\alpha\beta}(k) \\ \boldsymbol{y} & = \boldsymbol{C}\boldsymbol{X}(k+1) \end{cases} \tag{16}$$

where $\boldsymbol{A}_q = e^{AT_s}$ is state matrix,$\boldsymbol{B}_p = \int_0^{T_s} e^{A\tau}\boldsymbol{B}d\tau$ is input matrix, and $\boldsymbol{B}_{dp} = \int_0^{T_s} e^{A\tau}\boldsymbol{B}_i d\tau$ is disturbance matrix.

The voltage vector corresponding to each switching state of the inverter is shown in Table 1, and $v_j (j = \alpha, \beta)$ are the output voltages of the low-voltage side converter. Substituting v_j into (16) in turn, the predicted voltage at the $(k+1)$th instant time corresponding to each voltage vector can be obtained:

$$\begin{cases} \boldsymbol{X}(k+1) & = \boldsymbol{A}_q \boldsymbol{X}(k) + \boldsymbol{B}_p \boldsymbol{v}(k) + \boldsymbol{B}_{dp} \boldsymbol{I}_{o\alpha\beta}(k) \\ \boldsymbol{y} & = \boldsymbol{C}\boldsymbol{X}(k+1) \end{cases} \tag{17}$$

The corresponding output voltages performance cost function under each voltage vector control are shown in (18).

$$g_i = \left(U^*_{o\alpha}(k+1) - U_{o\alpha}(k+1)\right)^2 + \left(U^*_{o\beta}(k+1) - U_{o\beta}(k+1)\right)^2 + g_{ci} \tag{18}$$

where $U^*_{o\alpha}(k+1)$ and $U^*_{o\beta}(k+1)$ are the components of the output reference voltage under the α and β axes at the $(k+1)$th instant time.

$$g_{ci} = (I^*_{f\alpha}(k+1) - I_{f\alpha}(k+1))^2 + (I^*_{f\beta}(k+1) - I_{f\beta}(k+1))^2 \tag{19}$$

represents the cost function to control the short-circuit currents when a three-phase short-circuit fault occurs.

The calculation of the action time of the voltage vector and the synthesis of the equivalent voltage vector are similar to the TV-MPC control of rectifier stage. The action time of the voltage vector on the inverter stage and the synthesized equivalent voltage vector can be obtained as shown in (20) and (21).

$$\begin{cases} t_{i1} & = \frac{g_{i0}g_{i2}}{g_{i0}g_{i1}+g_{i0}g_{i2}+g_{i1}g_{i2}} T_s \\ t_{i2} & = \frac{g_{i0}g_{i1}}{g_{i0}g_{i1}+g_{i0}g_{i2}+g_{i1}g_{i2}} T_s \\ t_{i0} & = T_s - t_{i1} - t_{i2} \end{cases} \tag{20}$$

$$\begin{cases} u_{i\alpha-eq} & = \frac{t_{i1}}{T_s} v_{\alpha 1} + \frac{t_{i2}}{T_s} v_{\alpha 2} \\ u_{i\beta-eq} & = \frac{t_{i1}}{T_s} v_{\beta 1} + \frac{t_{i2}}{T_s} v_{\beta 2} \end{cases} \tag{21}$$

The structure diagram of the SST inverter stage TV-MPC control algorithm is shown in Fig. 4.

TABLE 2. Parameters of SST at all levels.

Parameter	Value	Parameter	Value
Grid side voltage	10 kV	LVDC bus voltage	600 V
Grid side resistance	0.1 Ω	Filter resistor	0.005 Ω
Grid side inductance	100 mH	Filter inductor	2.4 mH
HVDC bus voltage	15 kV	Filter capacitor	40 μF
Transformer Ratio	25:1	Output side voltage	380 V

IV. SIMULATION ANALYSIS

In this section, the effectiveness of the proposed TV-MPC and its performance comparison with FCS-MPC control and PI control are evaluated with simulation. Simulation tests are carried out by means of Matlab/Simulink using the model of Fig. 1 with parameters shown in Table 2. The sampling frequency of the whole control system is 10 kHz.

A. STEADY-STATE OPERATION

The simulation results of TV-MPC, FCS-MPC and PI three control algorithms are analyzed when SST is in steady state. Fig. 5 shows the waveform and THD of grid side currents. The THD under PI method and FCS-MPC are 2.05% and 1.69% respectively. The THD under the proposed TV-MPC is 0.52%, which has the lowest harmonic content among the three control methods. Comparing Figs. 6(a), 6(b), and 6(c), it can be seen that output voltages THD under three control methods are lower than the national standard by 5%. The harmonic under TV-MPC is only 0.52%, and the control performance of the output voltages quality has been significantly improved compared with FCS-MPC 0.95% and PI 1.73%.

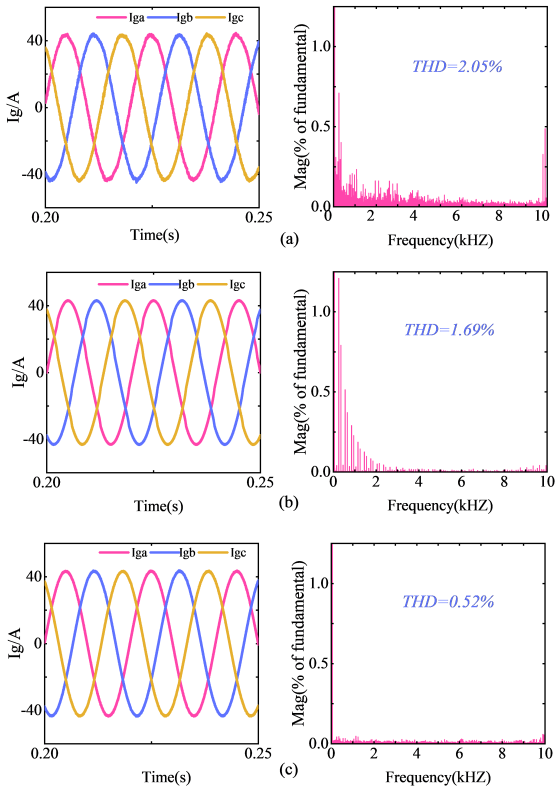

FIGURE 5. Grid side currents in steady state:(a) under the PI control (b) under the FCS-MPC control (c) under the proposed TV-MPC control.

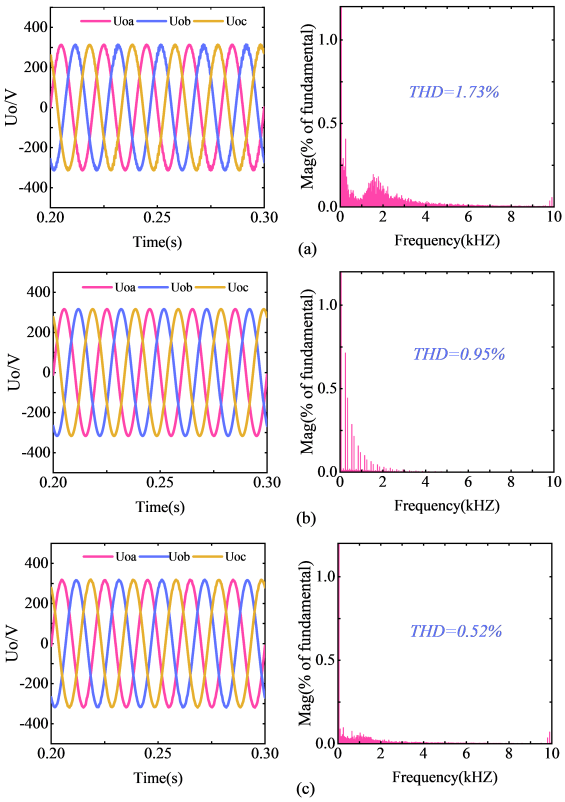

FIGURE 6. Output voltages in steady state:(a) under the PI control (b) under the FCS-MPC control (c) under the proposed TV-MPC control.

B. GRID SIDE VOLTAGES UNBALANCE

In the initial working condition, the rectifier stage of the solid-state transformer is connected to the 10 kV power grid, and the three-phase voltages are balanced. The A-phase voltage of grid side drops to 60% of the original voltage between 0.3 s and 0.4 s, resulting in an unbalance of the grid side voltages. The control effectiveness of TV-MPC, FCS-MPC and PI are verified respectively. Figs. 7(a), 7(b), and 7(c), it can be seen that the voltage comparing fluctuation of the high-voltage DC bus under PI control(5.3 V) is the largest and there is a certain steady-state error after returning to stability. Compared with PI control, the HVDC bus voltage fluctuation under FCS-MPC control(3 V) is smaller. The HVDC bus voltage under TV-MPC control has only a small fluctuation(0.8 V) and can quickly restore the reference voltage. By observing the simulation results of the power factor, the three controls basically meet the requirement that the grid side power factor of the SST works at unity power factor. And the power factor fluctuation under TV-MPC control is obviously smaller than that under FCS-MPC and PI control. Compared with the power simulation results in Fig. 7, the fluctuation of active and reactive power caused by the unbalanced grid side voltages cannot be effectively suppressed under PI control. The suppression of power fluctuation under FCS-MPC is better than that of PI control, while under TV-MPC control, the active power has only a small fluctuation, and the given reactive power can be accurately tracked, and the control effectiveness is significantly better than that of FCS-MPC and PI. It can also be seen that the grid side voltages unbalance of the SST under the three controls does not affect the output voltages. When the unbalance occurs, the voltage amplitude is always 311 V, a sine wave with a frequency of 50 Hz.

C. GRID SIDE VOLTAGES CONTAIN HARMONICS

At the moment of 0.3 s, the grid side voltages contain the positive sequence fifth harmonic and the positive sequence seventh harmonic. The control effectiveness of TV-MPC, FCS-MPC and PI are verified respectively. Comparing Figs. 8(a), 8(b), and 8(c), it can be seen that the HVDC bus voltage fluctuation under PI control is the largest and there is an overshoot before returning to stability. Compared with PI control, the fluctuation of the HVDC bus voltage under FCS-MPC control is smaller, the response speed is fast. The HVDC bus voltage under TV-MPC control fluctuates to a certain extent, and it can quickly recover to the rated reference voltage after the fault occurs. The fluctuation of active power and reactive power caused by harmonics cannot be effectively suppressed under PI control. The suppression of power fluctuation under FCS-MPC control is better than that of PI control. While under the control of TV-MPC, the power has a smaller fluctuation compared to FCS-MPC control. By comparing the waveform and THD of the output voltages during harmonic

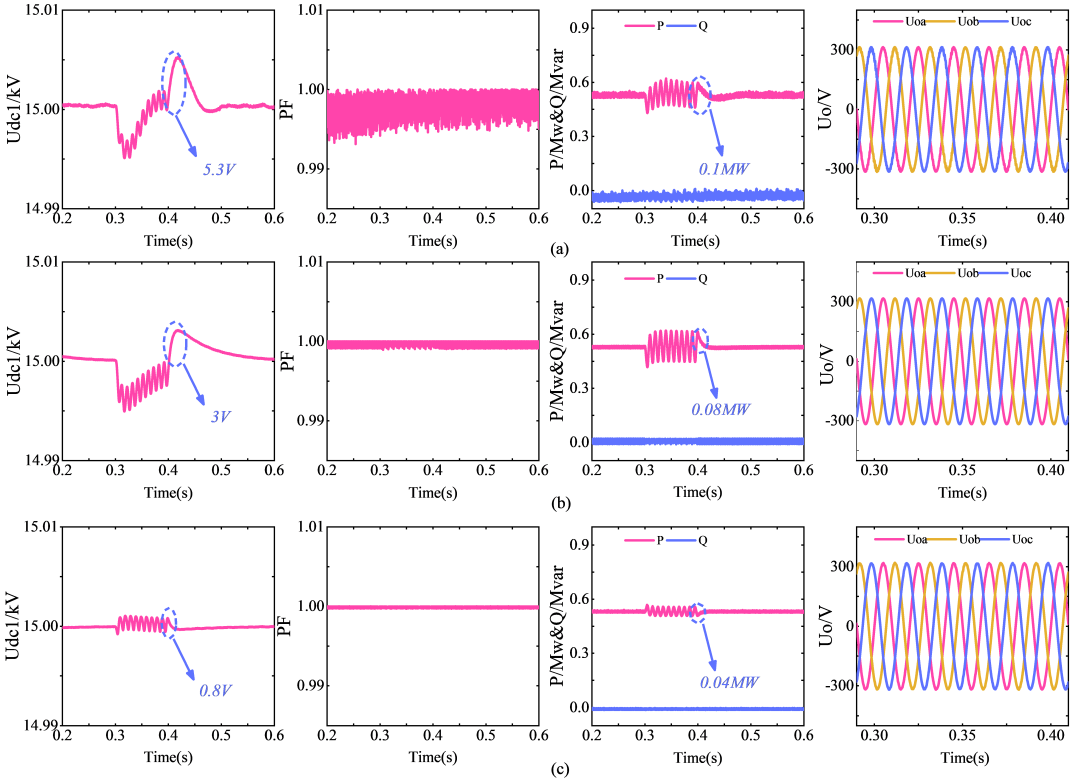

FIGURE 7. Grid side voltages unbalance: (a) under the PI control (b) under the FCS-MPC control (c) under the proposed TV-MPC control.

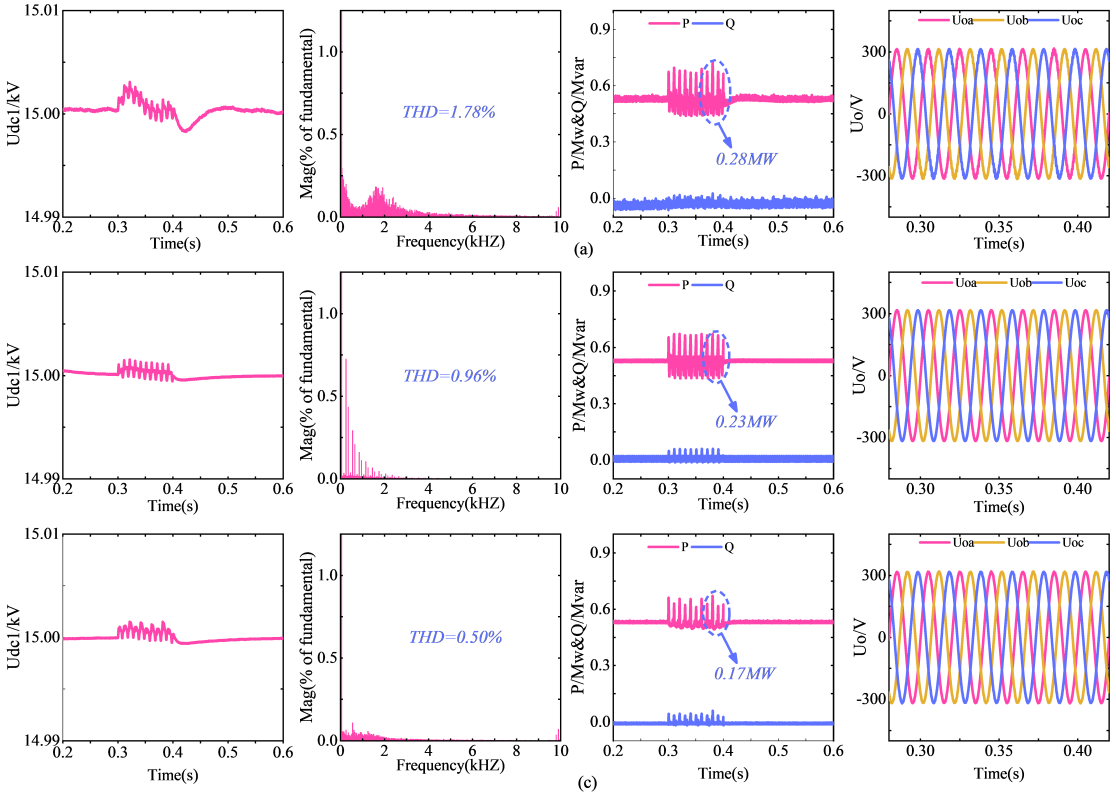

FIGURE 8. Grid side voltages contain harmonics: (a) under the PI control (b) under the FCS-MPC control (c) under the proposed TV-MPC control.

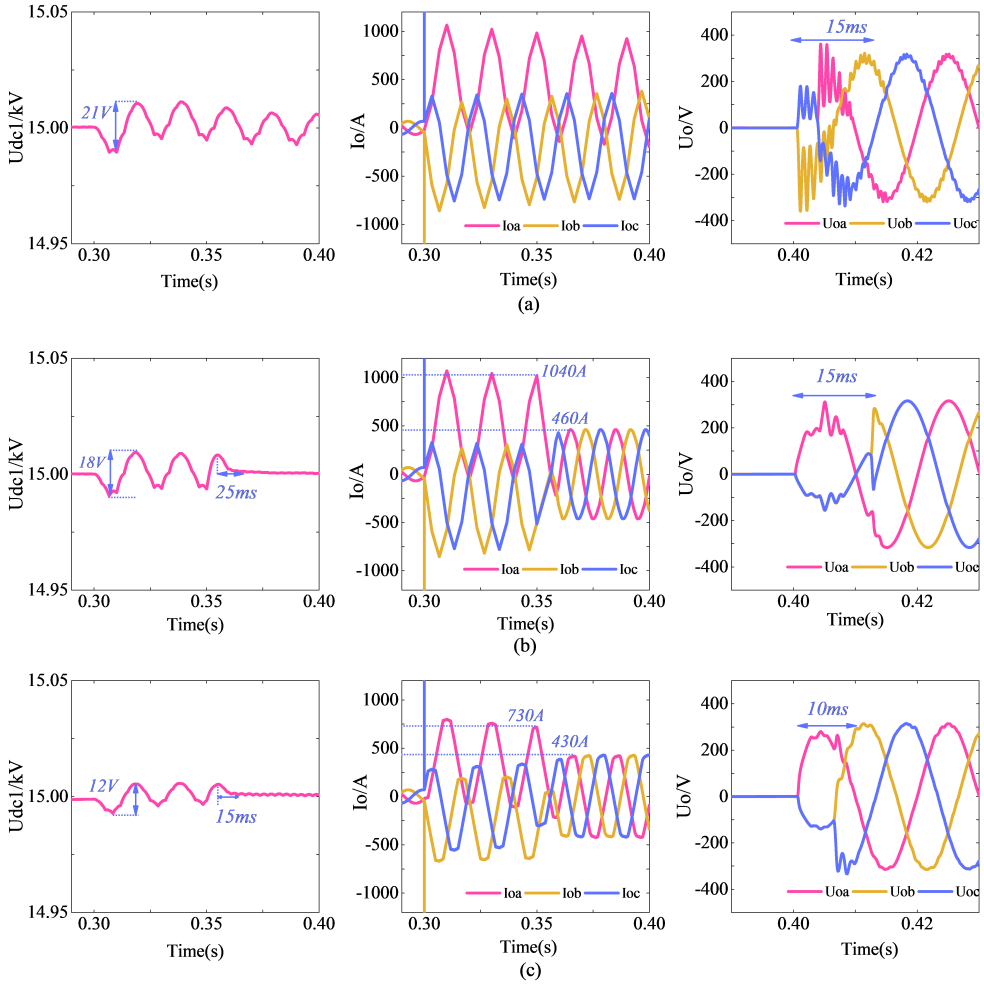

FIGURE 9. Three-phase short circuit: (a) under the PI control (b) under the FCS-MPC control (c) under the proposed TV-MPC control.

injection at the grid side with the output voltages under steady-state operation (see Fig. 6), it can be seen that all three control methods have a suppression effect on harmonics. Among them, the proposed TV-MPC method has the most obvious suppression effect with the THD of only 0.5%.

TABLE 3. The THD of output voltages and currents.

Measured variables	Control strategies	No-load	40 kW	80 kW	96 kW
I_o	FCS-MPC	—	0.66%	1.08%	1.76%
	TV-MPC	—	0.54%	0.86%	1.52%
U_o	FCS-MPC	0.95%	0.95%	1.32%	1.99%
	TV-MPC	0.42%	0.52%	1.15%	1.72%

D. THREE-PHASE SHORT CIRCUIT

A three-phase short-circuit fault occurred at the load side between 0.3 s and 0.4 s. Comparing Figs. 9(a), 9(b), and 9(c), it can be seen that under PI control, the HVDC bus voltage fluctuation reaches a maximum of 21 V, and there is little to no suppression of the huge currents generated by three-phase short-circuit. The HVDC bus voltage fluctuation under the FCS-MPC control is smaller than PI control, reaching 18 V. The short-circuit currents are controlled at 0.35 s, reducing from 1040 A to 460 A. Meanwhile, the HVDC bus voltage fluctuation is effectively suppressed and the dynamic time to the stable value is 25 ms. After the end of the three-phase short-circuit fault, the output voltages amplitude restored to the rated value in 15 ms. The HVDC bus voltage under TV-MPC control only fluctuates by 12 V. The output voltages are controlled only between 0.3 s and 0.35 s. The short-circuit currents are limited to 730 A, showing a better anti-interference performance than the FCS-MPC control (1040 A). The short-circuit currents are controlled at 0.35 s, reducing from 730 A to 430 A. Meanwhile, the HVDC bus voltage fluctuation is effectively suppressed, and the recovery time to the reference value is only 15 ms. After the end of the three-phase short-circuit fault, the output voltage amplitude is restored to the rated value in 10 ms. Comparing the time for the HVDC bus voltage to return to the reference value after adding the short-circuit currents control and the time for the output voltages amplitude to return to the rated value after the fault ends, it is clear that the TV-MPC control has a faster dynamic response than the FCS-MPC control.

TABLE 4. The dynamic time of output voltages and currents.

Measured variables	Control strategies	No-load	40 kW	80 kW	96 kW
I_o	FCS-MPC	—	3.1 ms	4.2 ms	5 ms
	TV-MPC	—	2 ms	3.4 ms	3.2 ms
U_o	FCS-MPC	0.9 ms	2 ms	4.1 ms	4.4 ms
	TV-MPC	0.6 ms	1.3 ms	3.2 ms	3.2 ms

TABLE 5. Comparison between TV-MPC, FCS-MPC and PI control schemes.

Cases	Parameters	TV-MPC	FCS-MPC	PI
Steady-state operation	THD of Grid side currents	0.52%	1.69%	2.05%
	THD of Output voltages	0.52%	0.95%	1.73%
Grid side voltages unbalance	Fluctuation of U_{dc1}	0.8 V	3 V	5.3 V
	Fluctuation of power factor	0.005	0.001	0.0003
	Fluctuation of active power	0.04 MW	0.08 MW	0.1 MW
Grid side voltages harmonics	THD of output voltages	0.5%	0.96%	1.78%
	Fluctuation of active power	0.17 MW	0.23 MW	0.28 MW
Three-phase short circuit	Fluctuation of U_{dc1}	12 V	18 V	21 V
	Short circuit currents (before 0.35 s)	730 A	1040 A	—
	Short circuit currents (after 0.35 s)	430 A	460 A	—
	Dynamic time of output voltages	10 ms	15 ms	15 ms

E. LOADS SUDDENLY CHANGE

The initial state of the SST load side is no-load operation. Putting 50% of load (40 kW) into operation at 0.1 s moment. Full load (80 kW) operating from 0.2 s to 0.3 s and finally operating over 20% of full load (96 kW). The THD of output voltages and currents are shown in Table 3. The output voltages and currents dynamic time of loads suddenly change are shown in Table 4.

V. CONCLUSION

Finite set model predictive control (FCS-MPC) shows competitive features in power converters control. However, its single vector action at each control interval limits its control performance. This paper has proposed a three-vector model predictive control (TV-MPC) with enhanced control performance. The traditional FCS-MPC control is improved by increasing the number of voltage vectors acting in one control interval to synthesize an equivalent vector. Simulation and comparison verification (See Table 3, Table 4 and Table 5) for five different operating conditions of SST at the grid side and load side lead to the following conclusions

1) At steady state, the output voltages of the SST has lower harmonic content under proposed TV-MPC compared to conventional FCS-MPC control and PI control. There is a large improvement in the regulation of the output voltages waveform quality.

2) The improved model predictive control can have better suppression effect on the fluctuation of SST high-voltage side converter power factor and DC bus voltage when faults occur on the grid side and load side. It has fast dynamic response and strong anti-interference property.

The improved model predictive control improves the control performance of the SST control system while meeting the SST control requirements. The regulation of power quality is achieved.

REFERENCES

[1] X. Yu, X. She, X. Ni, and A. Q. Huang, "System integration and hierarchical power management strategy for a solid-state transformer interfaced microgrid system," *IEEE Trans. Power Electron.*, vol. 29, no. 8, pp. 4414–4425, Aug. 2014.

[2] X. Yu, X. She, X. Zhou, and A. Q. Huang, "Power management for DC microgrid enabled by solid-state transformer," *IEEE Trans. Smart Grid*, vol. 5, no. 2, pp. 954–965, Mar. 2014.

[3] C. Tu, F. Xiao, Z. Lan, Q. Guo, and Z. Shuai, "Analysis and control of a novel modular-based energy router for DC microgrid cluster," *IEEE J. Emerg. Sel. Topics Power Electron.*, vol. 7, no. 1, pp. 331–342, Mar. 2019.

[4] D. Gonzalez-Agudelo, A. Escobar-Mejia, and H. Ramirez-Murrillo, "Dynamic model of a dual active bridge suitable for solid state transformers," in *Proc. 13th Int. Conf. Power Electron. (CIEP)*, Guanajuato, Mexico, Jun. 2016, pp. 350–355.

[5] L. Zhang, J. Qin, Y. Zou, Q. Duan, and W. Sheng, "Analysis of capacitor charging characteristics and low-frequency ripple mitigation by two new voltage-balancing strategies for MMC-based solid-state transformers," *IEEE Trans. Power Electron.*, vol. 36, no. 1, pp. 1004–1017, Jan. 2021.

[6] L. Wang, D. Zhang, Y. Wang, B. Wu, and H. S. Athab, "Power and voltage balance control of a novel three-phase solid-state transformer using multilevel cascaded H-bridge inverters for microgrid applications," *IEEE Trans. Power Electron.*, vol. 31, no. 4, pp. 3289–3301, Apr. 2016.

[7] X. She, R. Burgos, G. Wang, F. Wang, and A. Q. Huang, "Review of solid state transformer in the distribution system: From components to field application," in *Proc. IEEE Energy Convers. Congr. Expo. (ECCE)*, Raleigh, NC, USA, Sep. 2012, pp. 4077–4084.

[8] Q. Zhang, R. Callanan, M. K. Das, S.-H. Ryu, A. K. Agarwal, and J. W. Palmour, "SiC power devices for microgrids," *IEEE Trans. Power Electron.*, vol. 25, no. 12, pp. 2889–2896, Dec. 2010.

[9] S. Madhusoodhanan, A. Tripathi, D. Patel, K. Mainali, A. Kadavelugu, S. Hazra, S. Bhattacharya, and K. Hatua, "Solid-state transformer and MV grid tie applications enabled by 15 kV SiC IGBTs and 10 kV SiC MOSFETs based multilevel converters," *IEEE Trans. Ind. Appl.*, vol. 51, no. 4, pp. 3343–3360, Jul. 2015.

[10] X. Li, F. Wu, G. Yang, and H. Liu, "Improved modulation strategy for single-phase isolated quasi-single-stage AC–DC converter to improve current characteristics," *IEEE Trans. Power Electron.*, vol. 35, no. 4, pp. 4296–4308, Apr. 2020.

[11] X. Wang, J. Liu, S. Ouyang, T. Xu, F. Meng, and S. Song, "Control and experiment of an H-bridge-based three-phase three-stage modular power electronic transformer," *IEEE Trans. Power Electron.*, vol. 31, no. 3, pp. 2002–2011, Mar. 2016.

[12] H. Zhang, X. Zhu, J. Shi, L. Tan, C. Zhang, and K. Hu, "Study on PWM rectifier without grid voltage sensor based on virtual flux delay compensation algorithm," *IEEE Trans. Power Electron.*, vol. 34, no. 1, pp. 849–862, Jan. 2019.

[13] J. Qin and M. Saeedifard, "Predictive control of a modular multilevel converter for a back-to-back HVDC system," *IEEE Trans. Power Del.*, vol. 27, no. 3, pp. 1538–1547, Jul. 2012.

[14] F. A. Villarroel, J. R. Espinoza, M. A. Perez, R. O. Ramirez, C. R. Baier, D. Sbarbaro, J. J. Silva, and M. A. Reyes, "Stable shortest horizon FCS-MPC output voltage control in non-minimum phase boost-type converters based on input-state linearization," *IEEE Trans. Energy Convers.*, vol. 36, no. 2, pp. 1378–1391, Jun. 2021.
[15] X. Liu, L. Zhou, J. Wang, X. Gao, Z. Li, and Z. Zhang, "Robust predictive current control of permanent-magnet synchronous motors with newly designed cost function," *IEEE Trans. Power Electron.*, vol. 35, no. 10, pp. 10778–10788, Oct. 2020.
[16] Z. Zhang, M. T. Larijani, W. Tian, X. Gao, J. Rodriguez, and R. Kennel, "Long-horizon predictive current control of modular-multilevel converter HVDC systems," in *Proc. 43rd Annu. Conf. IEEE Ind. Electron. Soc.*, Oct. 2017, pp. 4524–4530.
[17] X. Liu, L. Qiu, W. Wu, J. Ma, Y. Fang, Z. Peng, and D. Wang, "Predictor-based neural network finite-set predictive control for modular multilevel converter," *IEEE Trans. Ind. Electron.*, vol. 68, no. 11, pp. 11621–11627, Nov. 2021.
[18] X. Zhang, G. Tan, T. Xia, Q. Wang, and X. Wu, "Optimized switching finite control set model predictive control of NPC single-phase three-level rectifiers," *IEEE Trans. Power Electron.*, vol. 35, no. 10, pp. 10097–10108, Oct. 2020.
[19] Y. Liu, Y. Liu, H. Abu-Rub, and B. Ge, "Model predictive control of matrix converter based solid state transformer," in *Proc. IEEE Int. Conf. Ind. Technol. (ICIT)*, Taipei, China, Mar. 2016, pp. 1248–1253.
[20] M. Tomlinson, H. D. T. Mouton, R. Kennel, and P. Stolze, "A fixed switching frequency scheme for finite-control-set model predictive control—Concept and algorithm," *IEEE Trans. Ind. Electron.*, vol. 63, no. 12, pp. 7662–7670, Dec. 2016.
[21] Y. Yang, H. Wen, and D. Li, "A fast and fixed switching frequency model predictive control with delay compensation for three-phase inverters," *IEEE Access*, vol. 5, pp. 17904–17913, 2017.
[22] R. P. Aguilera, P. Lezana, and D. E. Quevedo, "Finite-control-set model predictive control with improved steady-state performance," *IEEE Trans. Ind. Informat.*, vol. 9, no. 2, pp. 658–667, May 2013.
[23] C. R. Baier, R. O. Ramirez, E. I. Marciel, J. C. Hernandez, P. E. Melin, and E. E. Espinosa, "FCS-MPC without steady-state error applied to a grid-connected cascaded H-Bridge multilevel inverter," *IEEE Trans. Power Electron.*, vol. 36, no. 10, pp. 11785–11799, Oct. 2021.
[24] Y. Zhang and W. Xie, "Low complexity model predictive control—Single vector-based approach," *IEEE Trans. Power Electron.*, vol. 29, no. 10, pp. 5532–5541, Oct. 2014.
[25] Y. Zhang, W. Xie, Z. Li, and Y. Zhang, "Low-complexity model predictive power control: Double-vector-based approach," *IEEE Trans. Ind. Electron.*, vol. 61, no. 11, pp. 5871–5880, Nov. 2014.
[26] X. Wang and D. Sun, "Three-vector-based low-complexity model predictive direct power control strategy for doubly fed induction generators," *IEEE Trans. Ind. Electron.*, vol. 32, no. 1, pp. 773–782, Jan. 2017.
[27] M. Vijayagopal, P. Zanchetta, L. Empringham, L. de Lillo, L. Tarisciotti, and P. Wheeler, "Control of a direct matrix converter with modulated model-predictive control," *IEEE Trans. Ind. Appl.*, vol. 53, no. 3, pp. 2342–2349, May 2017.

CAN DING was born in Shandong, China. He received the B.S. and M.S. degrees in electrical engineering from Xi'an Jiao Tong University (XJTU), Xi'an, China, in 2005 and 2010, respectively, and the Ph.D. degree in electrical engineering from the Huazhong University of Science and Technology (HUST), Wuhan, China, in 2018.

HONGRONG ZHANG received the B.S. degree from the Suzhou Institute of Technology, Jiangsu University of Science and Technology, Suzhou, China, in 2021. He is currently pursuing the M.S. degree in electrical engineering with China Three Gorges University (CTGU). His research interests include solid state transformer and DC micro-networks.

YUNWEN CHEN received the B.S. degree from the North China University of Water Resources and Electric Power (NCWU), Zhengzhou, China, in 2019. She is currently pursuing the M.S. degree in electrical engineering with China Three Gorges University (CTGU). Her research interests include wind power grid and DC micro-networks.

GUANG PU received the B.S. degree from Chengdu University (CDU), Chengdu, China, in 2021. He is currently pursuing the M.S. degree in electrical engineering with China Three Gorges University (CTGU). His research interests include topology design of DC circuit breakers and flexible DC transmission technology.